










Cite this: *Phys. Chem. Chem. Phys.*,
2024, 26, 2332

Multi-spectroscopic study of electrochemically-formed oxide-derived gold electrodes†

Sara Boscolo Bibi, ^a Ahmed M. El-Zohry, ^{‡§*a} Bernadette Davies, ^{ab}
Vladimir Grigorev,^a Christopher M. Goodwin,^{¶a} Patrick Lömker, ^a
Alexander Holm,^{||a} Harri Ali-Löytty, ^c Fernando Garcia-Martinez,^d
Christoph Schlueter,^d Markus Soldemo, ^a Sergey Koroidov ^{*a} and
Tony Hansson^{*a}

Oxide-derived metals are produced by reducing an oxide precursor. These materials, including gold, have shown improved catalytic performance over many native metals. The origin of this improvement for gold is not yet understood. In this study, *operando* non-resonant sum frequency generation (SFG) and *ex situ* high-pressure X-ray photoelectron spectroscopy (HP-XPS) have been employed to investigate electrochemically-formed oxide-derived gold (OD-Au) from polycrystalline gold surfaces. A range of different oxidizing conditions were used to form OD-Au in acidic aqueous medium (H_3PO_4 , pH = 1). Our electrochemical data after OD-Au is generated suggest that the surface is metallic gold, however SFG signal variations indicate the presence of subsurface gold oxide remnants between the metallic gold surface layer and bulk gold. The HP-XPS results suggest that this subsurface gold oxide could be in the form of Au_2O_3 or $\text{Au}(\text{OH})_3$. Furthermore, the SFG measurements show that with reducing electrochemical treatments the original gold metallic state can be restored, meaning the subsurface gold oxide is released. This work demonstrates that remnants of gold oxide persist beneath the topmost gold layer when the OD-Au is created, potentially facilitating the understanding of the improved catalytic properties of OD-Au.

Received 21st August 2023,
Accepted 12th December 2023

DOI: 10.1039/d3cp04009g

rsc.li/pccp

1 Introduction

Gold as an electrode material has shown one of the highest activities and selectivities for CO_2 reduction to CO among polycrystalline metals.^{1,2} Oxide-derived metals are catalysts produced by reducing an oxide precursor. These materials often show enhanced catalytic properties towards CO_2 reduction compared to the pure polycrystalline metals.^{3–6} The CO_2 reduction activity

of oxide-derived gold (OD-Au) is higher than untreated metallic gold.^{7,8} Fundamental understanding of the reasons for the improved properties, in particular the role of oxygen, is still missing.⁵ A study comparing OD-Au to polyhedral gold nanoparticles has revealed the presence of metastable, highly-active surface structures due to defects created during the oxide reduction.⁹ However, a full explanation for the role of these defects in the enhanced catalytic activity of OD-Au is lacking. Furthermore, the presence and the role of possible subsurface oxide remnants has not been considered.

In order to bring more clarity about the OD-Au formation and its improved catalytic activity, the electrochemistry of gold needs to be considered. At water oxidation potentials, the gold surface is oxidized but there is no generally accepted understanding of gold oxide composition and the chemical processes at different anodic potentials. The following chemical compositions have been suggested: AuO , AuOH , AuOOH , Au_2O_3 , and $\text{Au}(\text{OH})_3$.^{10–19} The lack of consensus about the chemical composition of the electrochemically-formed (hydr-)oxides, as well as *in situ* changes of oxide compositions, prevents the fundamental understanding of the catalytic properties of gold.^{20,21}

Here, to investigate the electronic and chemical properties of the OD-Au, *operando* non-resonant sum frequency generation (SFG)^{22,23} was used to follow the electronic changes in gold

^a Department of Physics, AlbaNova University Center, Stockholm University, 10691 Stockholm, Sweden. E-mail: ahmed.elzohry@kfupm.edu.sa, sergey.koroidov@fysik.su.se, tony.hansson@fysik.su.se

^b Department of Materials and Environmental Chemistry, Stockholm University, Svante Arrhenius väg 16C, 114 18 Stockholm, Sweden

^c Surface Science Group, Photonics Laboratory, Tampere University, P.O. Box 692, FI-33014 Tampere University, Finland

^d Photon Science, Deutsches Elektronen-Synchrotron (DESY), 22607 Hamburg, Germany

† Electronic supplementary information (ESI) available. See DOI: <https://doi.org/10.1039/d3cp04009g>

‡ These authors contributed equally to this work.

§ Present address: Center for Integrative Petroleum Research, King Fahd University of Petroleum and Minerals, 31261 Dhahran, Kingdom of Saudi Arabia.

¶ Present address: ALBA Synchrotron, 08290 Cerdanyola del Valles, Spain.

|| Present address: Department of Materials and Environmental Chemistry, Stockholm University, Svante Arrhenius väg 16C, 114 18 Stockholm, Sweden.



surfaces formed under different OD-Au preparation conditions, and *ex situ* high-pressure X-ray photoelectron spectroscopy (HP-XPS)^{24,25} was used to gain chemical insight into the nature of the observed electronic changes. Saturation water vapour pressure (30 mbar) condition is needed to prevent water desorption from electrolyte, which may alter the state of the electrode.

To gain a deeper understanding of the electrochemical OD-Au formation, we performed optical SFG spectroscopic measurements while simultaneously applying electrochemical methods²⁶ [chronoamperometry (CA) and cyclic voltammetry (CV)]. This was done in an acidic aqueous medium (H_3PO_4 , pH = 1) using a wider range of oxidising potentials than what previously reported^{27–29} to create different oxide precursors for the subsequent reduction step. Our SFG data suggests that the OD-Au contains subsurface gold oxide remnants below the top-most metallic layer when the oxide precursors are generated at potentials above the initial stage of oxidation, while the electrochemical data confirms that the surface is metallic. This subsurface gold oxide affects the gold free electron distribution, resulting in a decrease in the SFG intensity. *Ex situ* HP-XPS is then used to characterize electrochemical OD-Au formation under similar conditions. To alter the composition of the electrode surfaces as little as possible, the chamber had a saturation background pressure of water. Our XPS spectra suggest the presence of Au(III) oxide, potentially in the form of Au_2O_3 or $\text{Au}(\text{OH})_3$, after the OD-Au formation, while the corresponding electrochemical data from the preparation indicates that the surface is metallic. This implies that the gold oxide is contained beneath the metallic surface, in agreement with the SFG and corresponding electrochemical data. The electrochemical data together with the information from the complementary spectroscopic techniques provides a more complete insight into the principal characteristics of the electrochemically-formed OD-Au, strongly suggesting the presence of subsurface Au(III) oxides. This has the potential to aid our understanding of the surface chemistry behind the OD-Aus improved properties for catalytic CO_2 reduction to CO .^{4,7,8}

2 Experimental details

2.1 Chemicals

Phosphoric acid, H_3PO_4 , (≥ 85 wt% in water) was purchased from Sigma Aldrich. The gold foil for the electrical connections (99.95%) was purchased from Alfa Aesar. Potassium ferricyanide, $\text{K}_3\text{Fe}(\text{CN})_6$, was purchased from ACS (99%), and a 5 mM solution was used to calibrate the gold pseudoreference electrode. The electrolyte consisted of a 1 M solution of H_3PO_4 , pH ≈ 1 . This electrolyte was chosen to prevent a quick degradation of the CaF_2 window in the SFG electrochemical cell (EC). Ultrapure water (Milli-Q) was used to prepare the solutions.

2.2 Gold electrode preparations for SFG measurements

The electrodes were composed of gold (200 nm) on top of titanium (10 nm) on a quartz substrate. Titanium was chosen as the adhesion layer for its stability in wide anodic potential ranges.³⁰ The electrodes [working electrode (WE), counter

electrode (CE), and reference electrode (RE) shown in Fig. S1a, ESI†] were fabricated using photolithography and double layer resist lift-off. As final step, the electrodes were cleaned in O_2 plasma for 3 minutes. The size of the WE was approximately 1.3 cm^2 , and the space between the WE and CE was 0.6 mm.

2.3 Electrochemical cell (EC) for SFG measurements

The EC used in this study (Fig. S1a, ESI†) is a custom thin layer electrochemical cell inspired by the work of Tong *et al.*³¹ The internal section consists of a CaF_2 window ($\text{Ø } 25 \text{ mm} \times 2 \text{ mm}$, both sides optically polished) above a quartz substrate. Three gold electrodes were deposited on the quartz plate, as described in *Gold electrode preparations for SFG measurements*. A Teflon spacer of thickness $25 \mu\text{m}$ was placed between the CaF_2 window and the quartz substrate to control the volume of the electrolyte solution, which was around $3 \mu\text{L}$. The electrolyte solution was pumped with a peristaltic pump (Ismatec Reglo ICC) which was set to change all the electrolyte in the EC every second.

All the potential values in this study are *versus* standard hydrogen electrode (SHE). The electrical characteristics of the EC have been compared to a standard system of three gold electrodes in bulk electrolyte. The electrochemical results compared well. The electrochemical characterization was performed using a BioLogic SP-200 potentiostat.

2.4 Electrochemical protocols for SFG measurements

Oxide-derived gold (OD-Au) is prepared electrochemically by first applying an oxidation potential to oxidise the gold, then a reduction potential to produce a metallic surface. Two protocols were used to investigate with SFG the generation of OD-Au under varied oxidation potentials. In the first protocol, the oxidation potential is varied by changing the oxidation limit to which the potential is swept during the CV scans. In the second, the OD-Au is formed prior to the SFG measurements using different fixed oxidation potentials, and then the CV measurements are performed in a fixed potential range where SFG is reversible.

The EC was at the open circuit potential (OCP) every time a protocol was started. Oxygen gas bubbles formed at strong oxidation potentials do not influence our measurements since the electrochemical flow cell flushes them away without affecting the SFG response. Surface roughening effects due to electrochemical treatments^{18,32} do not influence the SFG response.³³

2.4.1 Protocol 1: swept potential oxide preparation. Prior to each cyclic voltammetry (CV) measurement, electrochemical annealing³⁴ was done at 0.7 V vs. SHE for 30 seconds (chronoamperometry, CA) in H_3PO_4 , which provided reproducible CVs. This CA potential was chosen since there are not any oxidation peaks near this potential in the CVs. For the CV scan, the lower potential was 0.7 V and the upper potential was varied in the range between 1.5 to 2.5 V. CV scan rates of both 10 and 50 mV s^{-1} were used to compare the SFG signal of OD-Au produced with different scan rates. The results are presented in Fig. 1 and 3.

2.4.2 Protocol 2: fixed potential oxide preparation. The second protocol consists of three steps:



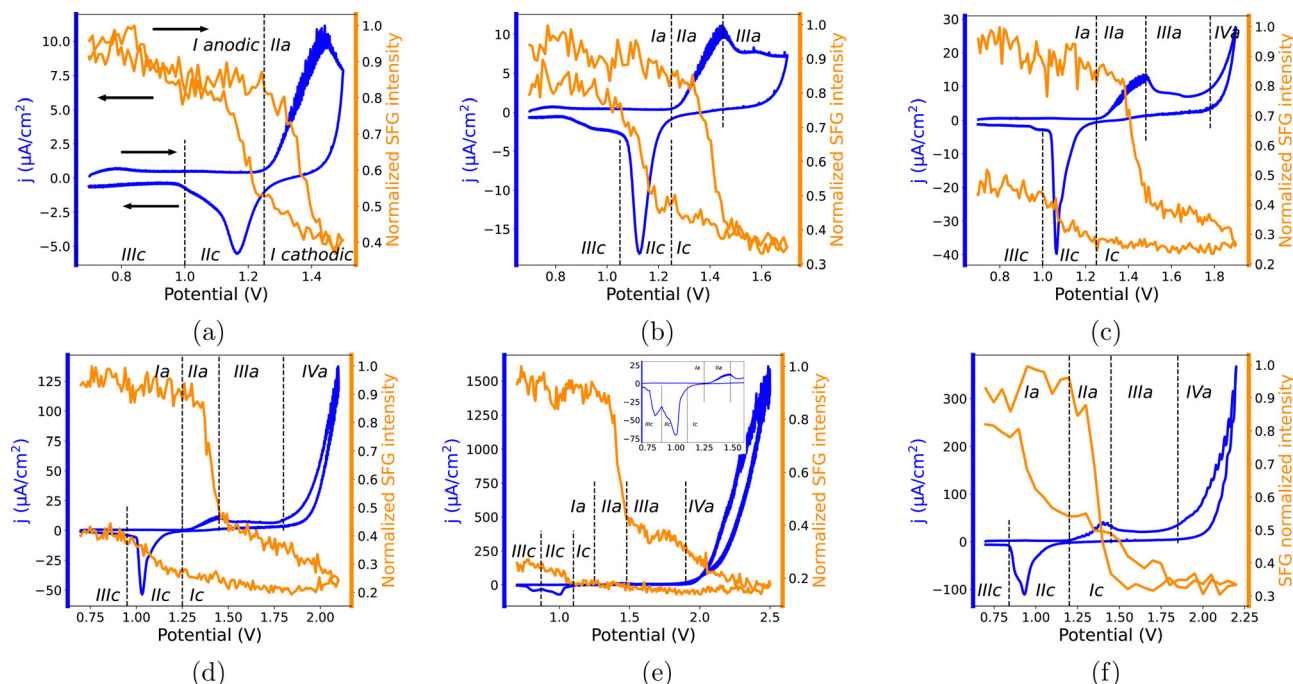


Fig. 1 (a)–(e) Combined SFG (orange) and CV (blue, scan rate 10 mV s^{-1} , potentials vs. SHE) measurements of gold in H_3PO_4 (pH = 1) for different upper potentials, the lower potential is 0.7 V for all measurements. The Roman numerals followed by 'a' (anodic) and 'c' (cathodic) indicate different regions of oxidation and reduction. More precisely, region Ia for the double-layer charging/pre-oxide formation, region IIa for the thin precursor of compact oxide formation, region IIIa for the compact oxide growth, and region IVa for hydrous oxide growth and the OER. Region Ic indicate the change of the sweep direction, which lowers the OER condition, and regions IIc and IIIc for the reduction of compact and hydrous oxide. The black arrows in (a) indicate the potential and SFG scanning directions. In (e) an inset shows a zoomed-in portion ($\times 3$) of the reduction part of the CV. (f) Combined SFG (orange) and CV (blue, scan rate 50 mV s^{-1} , potentials vs. SHE) measurements of gold in H_3PO_4 (pH = 1).

1. An oxidation step in which a specified potential in the range 0.5–2.5 V vs. SHE is held for 30 seconds (Fig. S3a and S4, ESI†). 0.7 V is the starting point, then this preparation potential is stepwise increased to 2.5 V, after that, decreased to 0.5 V. A milder oxidation potential is expected to produce a thinner oxide layer.

2. A reduction step by holding the potential at 0.7 V vs. SHE for 10 seconds (Fig. S3b, ESI†).

3. A surface characterization using the same CV parameters as in Fig. 1a (scan range 0.7–1.5 V vs. SHE and a scan rate of 10 mV s^{-1}) (Fig. 4a) in the thin oxide formation/reduction potential range simultaneously with SFG recording (Fig. 4c).

2.5 Laser system and SFG setup

The laser system used in this study was a standard commercial model for sum frequency generation purchased from Coherent. A Ti:sapphire system was used to generate 800 nm pulses with 40 fs pulse width and an average pulse energy of 4 mJ. Part of this output was converted into broadband pulses in the mid-IR region by an optical parametric amplifier and a non-collinear difference-frequency generator. A delay stage ensured the temporal overlap between the two beams at the electrode surface. A 750 nm short-pass edge filter let only the SFG signal from the EC enter the spectrometer (Andor SR-3031-A) and subsequently be detected by a charge coupled device (CCD) camera. The utilized IR pulses were centered at ca. 3500 nm, giving a SFG signal maximized at ca. 650 nm. All the beams were in *P* geometry.

For SFG, the input wavelengths are chosen such that there are no known resonances from adsorbates, including gold oxides, and thus the SFG is expected to mainly reflect the strong non-resonant response of neat gold (surface free-electron density).

2.6 HP-XPS measurements

HP-XPS measurements were conducted using the Polaris end-station³⁵ at the P22 beamline³⁶ of the Petra III synchrotron radiation facility at DESY (Hamburg, Germany). All HP-XPS spectra were collected using a photon energy of 7000 eV at a high-grazing incidence angle to increase surface sensitivity.³⁷ The gold sample is aligned for normal emission geometry with respect to the electron analyzer, X-ray grazing incidence angles 0.2° and 0.5° are used, which are below the critical angle for total external reflection (0.65° for Au at 7 keV)³⁸ in order to ensure surface sensitivity. During the characterization of the WE after electrochemical treatments water (Milli-Q[®]) was used to saturate the chamber pressure to around 30 mbar, which is the equilibrium vapor pressure of water at around 30, to prevent water desorption from the electrode. A three-electrode (all gold) cell configuration was used. The WE consisted of gold deposited on a rectangular silicon chip with a titanium adhesion layer, similar to the electrodes used in the SFG measurements. The WE was dipped together with the CE and RE (both gold foils) in a cuvette containing the electrolyte (H_3PO_4 , 1 M) for the electrochemical treatments. After each electrochemical treatment in 1 M H_3PO_4 , the WE was lifted, disconnected from



the potentiostat, and rinsed with Milli-Q[®] water. Then, it was moved to the experiment chamber to collect the HP-XPS spectra as quickly as possible (around 15 minutes), to prevent build-up of atmospheric contamination. The surface of the WE was maintained wet during the transfer to the chamber. The WE was electrically connected to the same ground potential as the analyzer front cone during all measurements. Survey spectra were gathered to probe for the presence of possible contaminants, Fig. S6 (ESI[†]) shows that C 1s was detected. A Shirley background³⁹ was subtracted from the Au 4f, while a Tougaard background⁴⁰ was subtracted for O 1s. The peak fitting model was done with Gaussian–Lorentzian peak shapes. The binding energy of our data in the Au 4f core-level region was calibrated considering the peak position of Au 4f_{7/2} from ref. 41 and the O 1s region was shifted accordingly. The recoil effect between the two regions was also calculated and included in the shift. For the gold oxide peaks in Au 4f, their integrated intensity ratio was locked to the branching ratio for f-orbitals (4:3). The contribution of H₂PO₄[−] shown in the O 1s spectra was calculated from the integrated intensity of P 1s and their photoionization cross-sections together with the stoichiometric amount within the salt (the P 1s spectra are shown in Fig. S7 (ESI[†]), a Shirley background was subtracted). The other contributions in the O 1s spectra were added based on the shape of the spectrum, and literature data of binding energies of the expected components were utilized. The same fitting parameters were used for all O 1s spectra.

3 Results and discussion

3.1 *In situ* spectroelectrochemical investigation

3.1.1 Swept-potential oxide preparation. Fig. 1 shows the simultaneously-recorded CV (blue) and integrated SFG intensity (orange) for gold in aqueous H₃PO₄ electrolyte at pH 1 for different upper potentials for OD-Au preparation in protocol 1 (see Section 2.4.1). The CV shape is typical of gold under acidic conditions.^{13,14,42} The concomitant SFG signal variation is very similar to what has been observed with second harmonic generation (SHG) using fundamental wavelengths in the near-infrared.^{27–29} Hence, the main SFG features in Fig. 1a can be attributed to the formation (region IIa) and reduction (region IIc) of the thin precursor of the compact oxide on the gold surface.^{14,15} This thin oxide modifies the surface electronic structure of the gold electrode and affects the SFG signal mainly by suppression of the surface free electron density.²⁷ At the end of the CV measurement, the SFG signal has recovered its initial intensity, suggesting that the gold recovers its metallic starting state in the double layer charging/pre-oxide formation region (regions Ia and IIc). This shows that the surface reduction/oxidation is, from the SFG point of view, fully reversible when the upper potential in the CV scan is limited to the region IIa (thin precursor of compact oxide formation). Herein, we define the reduction of SFG intensity at the highest anodic potential with respect to the intensity at the beginning of the measurement as the SFG drop, and the reduction in SFG signal between the end and beginning of the CV measurement as the SFG loss. For the reversible case in Fig. 1a they are 60% and 0%, respectively.

In literature, two types of oxides are reported to be produced when the oxidation of gold is achieved with strong oxidizing potentials: a compact oxide at lower potentials, followed by a hydrous one at higher potentials.^{14,42} Consensus about the chemical compositions and formation processes for both oxides is lacking. In agreement with this, Fig. 1b–e show that new features appear on the CV curve when the anodic potential range is extended beyond the thin oxide precursor formation (region IIa, 1.25–1.45 V) into a region of compact oxide growth (region IIIa, 1.45–1.8 V)^{14,42} then progressively to hydrous (less dense) oxide growth,^{11,13–15,18,42} and finally to the oxygen evolution reaction (OER, high positive current in region IVa at potentials higher than 1.8 V).^{11,13,14} During the cathodic scan, when the anodic potential is swept above 1.5 V (Fig. 1b–e), the reduction peak in region IIc shifts towards lower potentials and changes its intensity due to variations in composition and thickness of the oxides.^{11,13,14,18,32,43} In regions IIc (≈ 0.9 –1.25 V) and IIc (< 0.9 V) both compact and hydrous oxides get reduced from an electrochemical point of view.^{13,14,32,43} It is only when the potential region is extended into the strongly oxidizing region (2.5 V, region IVa in Fig. 1e) that the surface is not fully reduced back to metallic gold at the end of the CV scan, as indicated by the lingering faradaic current. It is important to note that each measurement is taken to start with a pure metallic surface without effects of previous scans, because there is no faradaic current during each preparation step as shown by the experimental CAs in Fig. S2 (ESI[†]).

In the SFG signal two main traits emerge when comparing Fig. 1a–e: first, SFG drop linearly increases in regions IIIa and IVa; second, SFG loss becomes more significant at the end of the scan with increasing anodic potentials. In all cases in Fig. 1a–e there is a steep SFG signal increase in region IIc. In Fig. 1a this SFG signal increase is seen to be connected to the reduction of the thin precursor of compact oxide. In Fig. 1e, as explained above, the CV has two negative peaks (regions IIc and IIc) indicating the reduction of both compact and hydrous oxides, and at the end of the CV measurement a small amount of faradaic current is present, indicating that the reduction process is not complete. Here, even if most of the (hydr)-oxide is reduced, the SFG is not recovered and the SFG loss is the highest among all the cases in Fig. 1a–e.

Both SFG drop and SFG loss trends depend on the CV scan rate. In Fig. 1f, the scan rate is five-fold higher than for Fig. 1a–e (50 mV s^{−1} vs. 10 mV s^{−1}). There is the same abrupt decrease of SFG intensity in region IIa, but in regions IIIa and IVa the SFG intensity is constant. Although the upper CV potential is well into OER range, now the SFG drop is lower than in Fig. 1d and e, and the SFG loss becomes almost negligible. The shape and position of the CV reduction peak in Fig. 1f indicates the presence of both compact and hydrous oxides,¹⁴ but, beyond the thin precursor of the compact oxide formation, these oxides do not affect the SFG signal, as shown in Fig. 1e. Thus, it suggests that the decrease in SFG signal in the range of multi-layer oxide growth¹³ (region IIIa onward in Fig. 1b–e) reflects a slow oxidation process that further lowers the metallic SFG response. It appears reasonable that this change in SFG response is related to the increased influence of



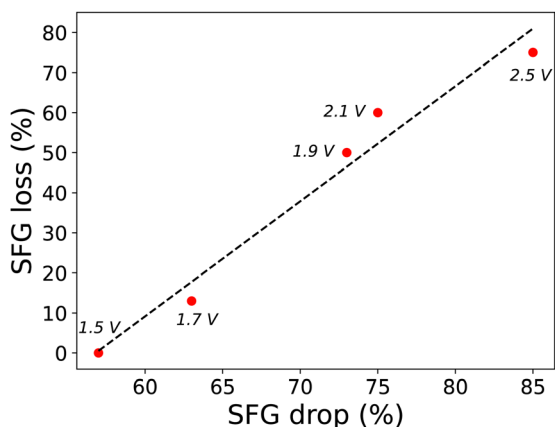


Fig. 2 SFG loss plotted vs. SFG drop for measurements in Fig. 1a–e. The potentials close to the red dots indicate the upper potential value for each CV range.

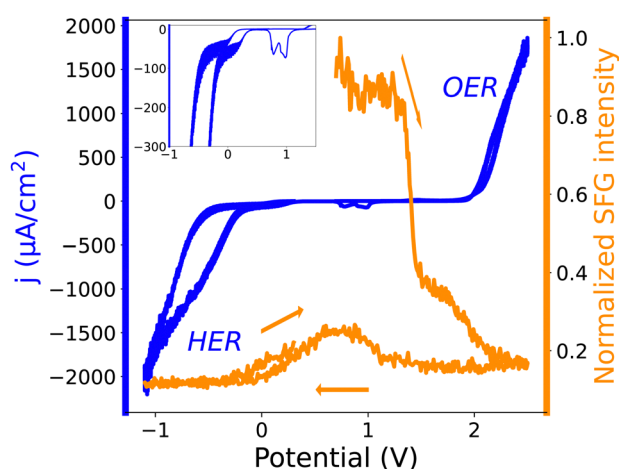


Fig. 3 Combined SFG (orange) and CV (blue, scan rate 10 mV s^{-1} , potentials vs. SHE) measurements of gold in H_3PO_4 ($\text{pH} = 1$). The inset on the top left of the figure zooms ($\times 3$) in the region from -0.6 to 1.6 V .

oxygen at the oxide/metal interface, while the other oxide multi-layers are too far from the interface to impact the SFG intensity.

After the initial oxidation event in region IIa, both SFG drop and SFG loss grow with increasing upper CV potential, and the two have a linear relationship (Fig. 2). This suggests that higher oxidizing conditions causes a higher SFG intensity depletion that is still present even after the surface oxide reduction occurs, as seen in Fig. 1b–e.

When the potential range is extended down to around -1 V (Fig. 3), the hydrogen evolution reaction (HER) occurs as indicated by the high negative current,^{44,45} implying that at least part of the surface is metallic gold.⁴⁶ Even after the HER, the SFG signal does not recover at the end of the scan, although the CV in Fig. 3 suggests that the surface is in its gold metallic state, as there is no faradaic current at the end of the measurement.

3.1.2 Fixed-potential oxide preparation. OD-Au can also be prepared using fixed potentials (protocol 2, see Section 2.4.2). For a range of different applied oxidation potentials (step 1), the resultant CVs and concomitant SFG signals (step 3) are shown in Fig. 4a and c, respectively. These CVs (Fig. 4a) all look qualitatively similar to those in Fig. 1a. A notable exception to this is when the initial oxidation (step 1) is done at 2.5 V (Fig. 4a green trace), in which case the CV starts with a reduction current and ends with a peak structure similar to that of the CV in Fig. 1e. This is attributed to an incomplete reduction process in step 2, as indicated by the negative current in the CA (Fig. S3b, ESI†). This incomplete reduction also manifests at the beginning of the CV (step 3) where the continued reduction of the surface hydrous oxide results in a negative initial current. The cathodic peaks at the end of the CV in Fig. 4a indicate that the initial continued reduction during the CV scan is ceased before completion and some hydrous oxide remains on the surface. The presence of the hydrous oxide also causes the negative shift of the main reduction peak similar to the one in Fig. 1e and, interestingly, a similar shift of the oxidation peak. For a preparation step of 2.2 V , the CV cycle ends with metallic gold even though it starts with a reducing current.

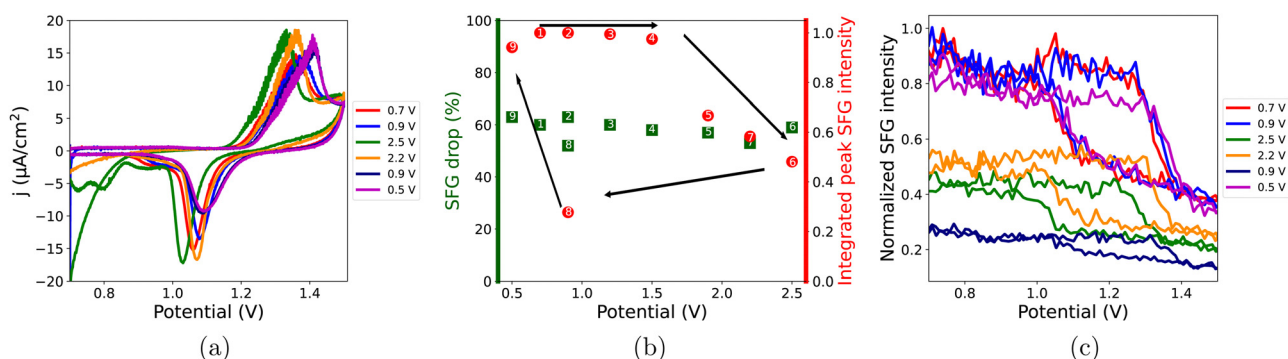


Fig. 4 (a) CVs (range 0.7 – 1.5 V vs. SHE, scan rate 10 mV s^{-1}) after doing the second electrochemical protocol. The legend and the black arrows shows the chronological order of some CA measurements from step 1. (b) Green squares: SFG drop collected after the chosen potentials in step 1 (across the full data set) are applied. Red circles: normalized SFG intensity at the end of the CVs; the normalization is to the SFG intensity when step 1 is 0.7 V (neat gold surface). The numbers (1–9) indicate the chronological order of the measurements. The x-axis indicates the CA potential in step 1 of the protocol. (c) Integrated potential-dependent SFG intensities collected during Fig. a (step 3), the normalization is done with respect to the SFG intensity from a neat gold surface (red curve, 0.7 V vs. SHE). The legend shows the chronological order of selected CA measurements vs. SHE during step 1.



The SFG intensity variations in Fig. 4c during the CV scans are in all cases consistent with that in Fig. 1a, with an SFG drop of about 50–60%, shown as green squares in Fig. 4b, and no SFG loss, indicative of the incipient oxidation and reduction of an initially metallic surface. There is a remarkable variation in the integrated peak SFG intensity for each CV scan, shown as red circles in Fig. 4b and SFG spectra in Fig. 4c, for preparation potentials (step 1) above 1.5 V. If this were due to an incomplete reduction process in step 2, as for 2.5 V, fewer metallic surface sites would be available during the next oxidation (thin gold oxide formation) and a diminished oxidation peak in the CV should be present. However, this cannot be the case here, because as seen in Fig. 4a, both oxidation and reduction peaks have similar intensities for all the different cases. Hence, the SFG intensity reduction (red circles in Fig. 4b) seems to occur without an oxide film present on the surface, except when step 1 is done at 2.5 V; but, as stated above, compact and hydrous oxides have negligible contribution to the SFG loss, which is also shown by the recovery of the SFG signal at the end of the CV cycle in Fig. 4c. This suggests that the oxygen atoms which are causing a reduced metallic SFG response, are mainly located below the surface, but close enough to the gold surface to affect the effective surface free electron density.

Fig. 4b shows the integrated SFG intensity of the measurements (step 3, protocol 2) in the order in which they were made. The potential in step 1 was progressively increased from measurement 4 to 7, the corresponding integrated SFG intensities from step 3 have a nearly linear relationship which matches the SFG drop in Fig. 1a–e. Then, the potential in step 1 was progressively decreased in measurements 8 and 9, to observe what happens to the gold surface when lower potentials are used again in step 1 after the high potentials of measurements 6 and 7. It is observed that the integrated SFG intensity after the preparation again at 0.9 V (Fig. 4b and c, point 8) is the lowest among all considered cases. This may be due to some rearrangement of the pre-existing subsurface gold oxide, which was not completely released in step 1, since 0.9 V is not high enough to provide any type of oxidation. Finally, when an initial oxidation potential of 0.5 V was applied (point 9) the SFG intensity is recovered. The corresponding CA current (Fig. S4, ESI†) shows a negative decay of the faradaic current due to the release of subsurface gold oxide.

Between the two OD-Au preparation protocols in this study, the gold oxide was reduced at different rates, which influences the restructuring of the gold surface.^{47,48} It has been previously shown that when the CV scan rate is slow (as in Fig. 1a–e and 3), there is diffusion of gold anions to the bulk electrolyte during oxidation conditions, leading to little redeposition of dissolved gold back to the surface of the electrode during the reduction process.^{32,47,49} Thus, it seems that in our CV procedure (Fig. 1a–e and 3) with a low reduction rate, only a small amount of gold is redeposited back onto the surface of the electrode during reduction. This turns the remaining surface oxide into subsurface oxide which is not well-protected by the new surface gold atoms^{47,48} and consequently it is easier to release the oxide with additional electrochemical treatments, resulting in a pure gold final state. On the other hand, when the oxidation is followed by

a high reduction rate corresponding to CA (as for step 2 in Fig. S3b and step 1 in Fig. S4, ESI†) there is substantial redeposition of gold on the electrode surface, leading to almost no gold loss in the electrolyte.⁴⁷ This means that more gold is deposited to create a new gold surface, which better protects/traps the oxide remnants in the subsurface. As a consequence, more time is needed to release this oxide. Currently, however, detailed mechanisms are missing.

3.2 Ex situ spectroelectrochemical investigation

To better understand the observed changes in SFG intensities during the electrochemical treatments, *ex situ* HP-XPS measurements were used to investigate metallic gold, oxidised gold and OD-Au formed under different preparation conditions. A saturation pressure of water vapour was kept in the analysis chamber for all measurements to prevent the gold (hydro-)oxide from getting reduced by the vacuum. In Fig. 5, XPS spectra of the gold electrode before (Fig. 5c and d) and after oxidation (Fig. 5a and b) are shown. The electrode was oxidized by (i) CA at 0.7 V for 20 seconds, (ii) CV between 0.7 V and 2.2 V with a scan rate of 10 mV s^{−1}, and (iii) CA at 2.5 V for 50 seconds. In the Au 4f core-level region, the metallic electrode prior oxidation shows only the two expected 5/2 and 7/2 spin-orbit components with the intensity branching ratio of 3/4. While the oxidized electrode, after a proper deconvolution, features two additional intensities namely gold in oxidation state +3 (85.6 and 89.9 eV),^{18,41,50–54}

The contributions from this oxidation state was set to hold the same spin-orbit split as the metallic gold. In the O 1s region, for metallic gold only water contribution is observed, adsorbed or multilayer, while for the oxidized gold electrode, multiple components are readily seen. Peak deconvolution requires the following components: oxide (~530.0 eV), hydroxide (~531.0 eV), adsorbed water (~531.8 eV), phosphate (H₂PO₄[−]) (~532.5 eV),

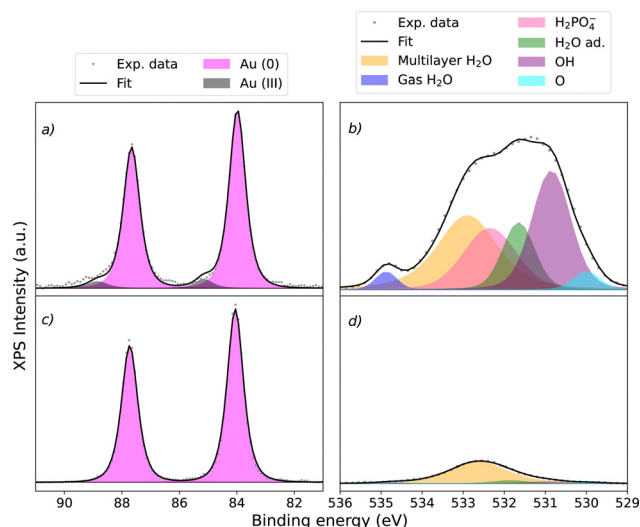


Fig. 5 HP-XPS spectra for Au 4f (a) and (c) and O 1s (b) and (d). $h\nu = 7000$ eV, grazing incidence angle 0.2°. Bottom (c) and (d): Before oxidation. Top (a) and (b): After electrochemical treatment (CA at 0.7 V for 20 second, CV between 0.7 and 2.2 V with a scan rate of 10 mV s^{−1}, and CA at 2.5 V for 50 seconds).



multilayer water (~ 532.5 eV), and gas-phase water.^{55–58} Both the oxide and hydroxide components correspond to the oxide peak in Au 4f. In literature, the following gold (hydr)-oxide compounds have been suggested: Au_2O_3 , AuOOH and $\text{Au}(\text{OH})_3$ for $\text{Au}(\text{III})$.^{14,18,19,59} The Au_2O_3 has two non-equivalent oxygen sites, giving rise to the presence of two components at 529.1 and 530.0 eV.⁶⁰ In this study, the experimental resolution does not permit such fine discrimination of components. The phosphate signal in the oxygen region is determined by the stoichiometric amount within the salt. As a result the spectroscopic signal of the O 1s component of the phosphate is determined by the P 1s peak intensity (not shown here).

The formation of OD-Au requires an oxidation–reduction cycle. For the XPS investigation, the OD-Au was prepared electrochemically *ex situ via* (i) CA at 0.7 V for 20 seconds, (ii) CV from 0.7 V to 2.2 V with a scan rate of 10 mV s^{-1} , (iii) CA at 2.5 V for 50 seconds, and (iv) CA at 0.7 V for 25 seconds. Fig. S5 (ESI[†]) shows the CAs for the last two steps of this protocol, proving that at the end the surface oxide is fully reduced from an electrochemical point of view. This means similar conditions to the preparation in Fig. 4 point 6. The HP-XPS spectra of OD-Au are shown in Fig. 6a and b. To increase the information depth to probe oxide species below the surface after OD-Au formation, the grazing incidence angle was increased to 0.5° . The XPS Au 4f spectrum of OD-Au (Fig. 6a) exhibits a small increase of intensities at 85.6 and 89.9 eV compared to pure metallic gold, the intensities are from the spin-orbit components of Au in oxidation state +3. The O 1s region for OD-Au (Fig. 6b) was modelled with the same components for the peak deconvolution as the oxidized gold electrode. Contributions from both oxide (cyan) and hydroxide (purple) species are present in this O 1s spectrum, and their relative intensity ratio is 0.36, lower than the oxide-to-hydroxide ratio in Fig. 5 of 0.10. This

suggests that the Au_2O_3 is more stable than $\text{Au}(\text{OH})_3$ under reductive conditions. As the CA shows metallic surface for OD-Au, it is reasonable to suggest this Au_2O_3 is located beneath a layer of metallic gold, similarly to what was found by Wang *et al.* for OD-Cu, where oxide remnants beneath the metallic copper after reduction were observed.⁶¹ In contrast to the Wang *et al.* study of OD-Cu, this XPS OD-Au study was conducted with a water film on the surface, which does not permit resolving the presence of subsurface oxygen atoms.

The XPS data supports that there are (hydro)-oxide remnants in OD-Au. Despite the electrochemical measurements suggesting that the surface is metallic (fully reduced), here XPS data suggests that the oxide is buried beneath a layer of metallic gold. The presence of such subsurface gold oxides can explain the changes in SFG intensity, as they depend on the local electronic structure on the gold film. Furthermore, the presence of oxide remnants in OD-Au may help in constructing a more complete understanding of the enhanced catalytic properties of OD-Au over metallic gold for CO_2 reduction to CO.

4 Conclusions

This study compares electrochemical data, SFG signals, and XPS spectra of untreated metallic gold, oxidized gold, and oxide-derived gold (OD-Au) electrodes. While the electrochemical data for OD-Au suggests that the electrode's surface is metallic, both SFG and XPS show that the electrode is altered from the untreated metallic state. The changes in the SFG signal variations suggest that subsurface remnants of the electrochemically formed (hydr)-oxides affect the surface electronic structure. The XPS data identifies these remnants in OD-Au to be Au_2O_3 and $\text{Au}(\text{OH})_3$. The presence of these oxide remnants affect the surface free electron density of (OD-Au) electrodes. Further investigations are needed to elucidate the mechanistic details behind the formation of the (hydr)-oxide remnants, which might explain the improved catalytic performance for CO_2 reduction of OD-Au materials over their metallic counterpart reported in literature.

Conflicts of interest

There are no conflicts to declare.

Acknowledgements

This research was supported by the Knut and Alice Wallenberg Foundation under Grant No. 2016.0042, the Swedish Research Council (2019-05114) and WISE-ap1 provided to Dr Sergey Koroidov, and by the Academy of Finland Flagship Programme, Photonics Research and Innovation (PREIN) (decision number 320165) and by the Jane & Aatos Erkkö Foundation (project “Solar Fuels Synthesis”) provided to Dr Harri Ali-Löytty. The authors wish to thank Dr Taras Golod for preparing the gold electrodes, and Dr Matthias Hudl Waltn and Dr Henrik Öström for helping with the laser maintenance and support at the laser lab at AlbaNova University Center (Stockholm, Sweden). The

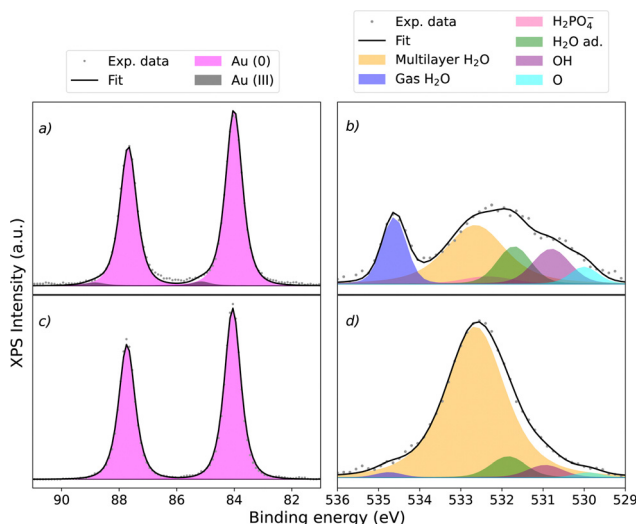


Fig. 6 HP-XPS spectra for Au 4f (a) and (c) and O 1s (b) and (d). $h\nu = 7000$ eV, grazing incidence angle 0.5° . Bottom (c) and (d): Before electrochemical treatment; top (a) and (b): OD-Au electrochemical treatment (CA at 0.7 V for 30 second, linear sweep voltammetry from 0.7 to 2.5 V with a scan rate of 10 mV s^{-1} , CA at 2.5 V for 50 seconds, and CA at 0.7 V for 25 seconds).



authors also acknowledge DESY (Hamburg, Germany), a member of the Helmholtz Association HGF, for the provision of experimental facilities. Parts of this research were carried out at PETRA III using beamline P22 and we would like to thank Ilja Schostak for assistance. Beamtime was allocated for proposal I-20221301EC.

Notes and references

- Y. Hori, A. Murata, K. Kikuchi and S. Suzuki, *J. Am. Chem. Soc., Chem Commun.*, 1987, 728–729.
- Y. Hori, in *Modern Aspects of Electrochemistry*, ed. C. G. Vayenas, R. E. White and M. E. Gamboa-Aldeco, Springer, New York, New York, NY, 2008, vol. 42, pp. 89–189.
- M. Ma, B. J. Trzesniewski, J. Xie and W. A. Smith, *Angew. Chem., Int. Ed.*, 2016, 55, 9748–9752.
- H. Kim, H. S. Park, Y. J. Hwang and B. K. Min, *J. Phys. Chem. C*, 2017, 121, 22637–22643.
- J. E. Pander, D. Ren, Y. Huang, N. W. X. Loo, S. H. L. Hong and B. S. Yeo, *ChemElectroChem*, 2018, 5, 219–237.
- N. J. Firet, M. A. Blommaert, T. Burdyny, A. Venugopal, D. Bohra, A. Longo and W. A. Smith, *J. Mater. Chem. A*, 2019, 7, 2597–2607.
- Y. Chen, C. W. Li and M. W. Kanan, *J. Am. Chem. Soc.*, 2012, 134, 19969–19972.
- Z. Qi, J. Biener and M. Biener, *ACS Appl. Energy Mater.*, 2019, 2, 7717–7721.
- X. Min, Y. Chen and M. W. Kanan, *Phys. Chem. Chem. Phys.*, 2014, 16, 13601–13604.
- R. G. P. Giron and G. S. Ferguson, *J. Electrochem. Soc.*, 2019, 166, H47–H53.
- G. Tremiliosi-Filho, L. Dall'Antonia and G. Jerkiewicz, *J. Electroanal. Chem.*, 1997, 422, 149–159.
- B. E. Conway, B. Barnett, H. Angerstein-Kozłowska and B. V. Tilak, *J. Chem. Phys.*, 1990, 93, 8361–8373.
- O. Diaz-Morales, F. Calle-Vallejo, C. de Munck and M. T. M. Koper, *Chem. Sci.*, 2013, 4, 2334–2343.
- S. Xia and V. Birss, *J. Electroanal. Chem.*, 2001, 500, 562–573.
- M. Tian, W. G. Pell and B. E. Conway, *Electrochim. Acta*, 2003, 48, 2675–2689.
- G. Tremiliosi-Filho, L. Dall'Antonia and G. Jerkiewicz, *J. Electroanal. Chem.*, 2005, 578, 1–8.
- H. Angerstein-Kozłowska, B. Conway, A. Hamelin and L. Stoicoviciu, *Electrochim. Acta*, 1986, 31, 1051–1061.
- M. Peuckert, F. Coenen and H. Bonzel, *Surf. Sci. Lett.*, 1984, 141, 515–532.
- S. Yang and D. G. H. Hetterscheid, *ACS Catal.*, 2020, 10, 12582–12589.
- C. Bürgel, N. M. Reilly, G. E. Johnson, R. Mitric, M. L. Kimble, A. W. Castleman and V. Bonačić-Koutecký, *J. Am. Chem. Soc.*, 2008, 130, 1694–1698.
- Y. Odarchenko, D. J. Martin, T. Arnold and A. M. Beale, *Faraday Discuss.*, 2018, 208, 243–254.
- Y. R. Shen, *Fundamentals of Sum-Frequency Spectroscopy*, Cambridge University Press, Cambridge, 2016.
- Y. R. Shen, *J. Chem. Phys.*, 2020, 153, 180901.
- J. F. Moudler, W. F. Stickle, P. E. Sobol and K. D. Bomben, *Handbook of X-ray Photoelectron Spectroscopy*, sergey, 1992.
- A. Nilsson, *J. Electron Spectrosc. Relat. Phenom.*, 2002, 126, 3–42.
- A. J. Bard and L. R. Faulkner, *Electrochemical methods: fundamentals and applications*, Wiley, New York, 2nd edn, 2001.
- P. Guyot-Sionnest and A. Tadjeddine, *J. Chem. Phys.*, 1990, 92, 734–738.
- S. M. Baten, A. G. Taylor and C. P. Wilde, *Electrochim. Acta*, 2008, 53, 6829–6834.
- I. Nahalka, G. Zwaschka, R. K. Campen, A. Marchioro and S. Roke, *J. Phys. Chem. C*, 2020, 124, 20021–20034.
- J. Hoogvliet and W. van Bennekom, *Electrochim. Acta*, 2001, 47, 599–611.
- Y. Tong, F. Lapointe, M. Thämer, M. Wolf and R. K. Campen, *Angew. Chem., Int. Ed.*, 2017, 56, 4211–4214.
- S. Cherevko, A. A. Topalov, I. Katsounaros and K. J. Mayrhofer, *Electrochem. Commun.*, 2013, 28, 44–46.
- M. J. Dignam and M. Moskovits, *J. Chem. Soc., Faraday Trans. 2*, 1973, 69, 65–78.
- B. Conway, *Prog. Surf. Sci.*, 1995, 49, 331–452.
- P. Amann, D. Degerman, M.-T. Lee, J. D. Alexander, M. Shipilin, H.-Y. Wang, F. Cavalca, M. Weston, J. Gladh, M. Blom, M. Björkhage, P. Löfgren, C. Schlueter, P. Loemker, K. Ederer, W. Drube, H. Noei, J. Zehetner, H. Wentzel, J. Åhlund and A. Nilsson, *Rev. Sci. Instrum.*, 2019, 90, 103102.
- C. Schlueter, A. Gloskovskii, K. Ederer, I. Schostak, S. Piec, I. Sarkar, Y. Matveyev, P. Lömker, M. Sing, R. Claessen, C. Wienmann, C. Schneider, K. Medjanik, G. Schönhense, P. Amann, A. Nilsson and W. Drube, *AIP Conf. Proc.*, 2019, 2054, 040010.
- C. M. Goodwin, M. Shipilin, S. Albertin, U. Hejral, P. Lömker, H.-Y. Wang, S. Blomberg, D. Degerman, C. Schlueter, A. Nilsson, E. Lundgren and P. Amann, *J. Phys. Chem. Lett.*, 2021, 12, 4461–4465.
- Henke, X-ray database of Center for X-Ray Optics, Berkeley National Laboratory (USA), https://henke.lbl.gov/optical_constants.
- D. A. Shirley, *Phys. Rev. B: Condens. Matter Mater. Phys.*, 1972, 5, 4709–4714.
- S. Tougaard, *J. Vac. Sci. Technol., A*, 2021, 39, 011201.
- A. Thompson, I. Lindau, D. Attwood, Y. Liu, E. Gullikson, P. Pianetta, M. Howells, A. Robinson, K. Kim, J. Scofield, J. Kirz, J. Underwood, J. Kortright, G. Williams and H. Winick, *X-ray data booklet*, Lawrence Berkeley National Laboratory, University of California, Berkeley, CA, 2009, 94720.
- L. D. Burke and P. F. Nugent, *Gold Bull.*, 1997, 30, 43–53.
- B. Conway, *J. Electroanal. Chem.*, 2002, 524–525, 4–19.
- M. C. O. Monteiro, F. Dattila, B. Hagedoorn, R. García-Muelas, N. López and M. T. M. Koper, *Nat. Catal.*, 2021, 4, 654–662.
- C. J. Bondue, M. Graf, A. Goyal and M. T. M. Koper, *J. Am. Chem. Soc.*, 2021, 143, 279–285.
- Y. Xu, *Int. J. Hydrogen Energy*, 2009, 34, 77–83.
- C. Stumm, S. Grau, F. D. Speck, F. Hilpert, V. Briega-Martos, K. Mayrhofer, S. Cherevko, O. Brummel and J. Libuda, *J. Phys. Chem. C*, 2021, 125, 22698–22704.



- 48 C. Köntje, D. M. Kolb and G. Jerkiewicz, *Langmuir*, 2013, **29**, 10272–10278.
- 49 S. Cherevko, A. A. Topalov, A. R. Zeradjanin, I. Katsounaros and K. J. J. Mayrhofer, *RSC Adv.*, 2013, **3**, 16516.
- 50 T. Dickinson, A. F. Povey and P. M. A. Sherwood, *J. Chem. Soc., Faraday Trans. 1*, 1975, **71**, 298.
- 51 K. Juodkazis, J. Juodkazyte, V. Jasulaitiene, A. Lukinskas and B. Sebek, *Electrochem. Commun.*, 2000, **2**, 503–507.
- 52 B. Koslowski, R. Wahrenberg and P. Oelhafen, *Surf. Sci.*, 2001, **475**, 1–10.
- 53 A. Y. Klyushin, T. C. R. Rocha, M. Hävecker, A. Knop-Gericke and R. Schlögl, *Phys. Chem. Chem. Phys.*, 2014, **16**, 7881–7886.
- 54 E. Artmann, L. Forschner, K. M. Schüttler, M. Alâ-Shakran, T. Jacob and A. K. Engstfeld, *ChemPhysChem*, 2023, **24**, e202200645.
- 55 P. M. A. Sherwood, *Surf. Sci. Spectra*, 2002, **9**, 62–66.
- 56 A. I. Stadnichenko, S. V. Koshcheev and A. I. Boronin, *Moscow Univ. Chem. Bull.*, 2007, **62**, 343–349.
- 57 H. S. Casalongue, S. Kaya, V. Viswanathan, D. J. Miller, D. Friebe, H. A. Hansen, J. K. Nørskov, A. Nilsson and H. Ogasawara, *Nat. Commun.*, 2013, **4**, 2817.
- 58 H. Ali-Löytty, M. W. Louie, M. R. Singh, L. Li, H. G. Sanchez Casalongue, H. Ogasawara, E. J. Crumlin, Z. Liu, A. T. Bell, A. Nilsson and D. Friebe, *J. Phys. Chem. C*, 2016, **120**, 2247–2253.
- 59 M. T. M. Koper, *Chem. Sci.*, 2013, **4**, 2710–2723.
- 60 A. I. Stadnichenko, S. V. Koshcheev and A. I. Boronin, *J. Struct. Chem.*, 2015, **56**, 557–565.
- 61 H.-Y. Wang, M. Soldemo, D. Degerman, P. Lömker, C. Schlueter, A. Nilsson and P. Amann, *Angew. Chem., Int. Ed.*, 2022, **61**, e202111021.

